Interfacial characterization and bonding mechanism of W/ODS-316 L steel multi-material structure fabricated by laser powder bed fusion

Xie, Zhirong; Zhou, Yan; Wang, Xiaoqiang; Chen, Keyu; Wang, Ruifang; Wen, Shifeng; Che, Yusi; Shi, Yusheng; He, Jilin

DOI
10.1016/j.matchar.2024.114242

Publication date
2024

Document Version
Final published version

Published in
Materials Characterization

Citation (APA)
Xie, Z., Zhou, Y., Wang, X., Chen, K., Wang, R., Wen, S., Che, Y., Shi, Y., & He, J. (2024). Interfacial characterization and bonding mechanism of W/ODS-316 L steel multi-material structure fabricated by laser powder bed fusion. *Materials Characterization*, *216*, Article 114242. https://doi.org/10.1016/j.matchar.2024.114242

Materials Characterization 216 (2024) 114242

Contents lists available at ScienceDirect

Materials Characterization

journal homepage: www.elsevier.com/locate/matchar

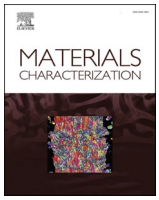

Interfacial characterization and bonding mechanism of W/ODS-316 L steel multi-material structure fabricated by laser powder bed fusion

Zhirong Xie [a], Yan Zhou [b,*], Xiaoqiang Wang [c], Keyu Chen [d], Ruifang Wang [a], Shifeng Wen [c], Yusi Che [a,*], Yusheng Shi [c], Jilin He [a]

[a] School of Material Science and Engineering, Zhengzhou University, Zhengzhou 450001, China
[b] National Center of Technology Innovation for Digital Construction, School of Civil and Hydraulic Engineering, Huazhong University of Science and Technology, Wuhan 430074, China
[c] State Key Laboratory of Material Processing and Die & Mould Technology, School of Materials Science and Engineering, Huazhong University of Science and Technology, Wuhan 430074, China
[d] Department of Biomechanical Engineering, Delft University of Technology, Delft, 2628 CD, South Holland, Netherlands

ARTICLE INFO

Keywords:
Laser powder bed fusion(L-PBF)
W/ODS steel multi-material
Interfacial characterization
Bonding mechanism

ABSTRACT:

Oxide dispersion strengthened(ODS) steels and W play an important role in plasma facing components(PFCs). However, complex multi-material structures in PFCs are manufactured by assembling discrete components using conventional techniques and subsequently fused together by a welding process, which creates weak interface zones with limited performance. In this study, a W/ODS-316L multi-material structures were integrally fabricated utilizing the laser powder bed fusion (LPBF) methodology. The study delves into the examination of interfacial diffusion characteristics, the underlying interfacial bonding mechanism, and the mechanical properties of the fabricated structures. The results showed that a good metallurgical bond in W/ODS-316L multi-material interfaces was attributed to Marangoni convection and the development of a keyhole during the forming process. These phenomena induced intensive elemental diffusion across the interface, resulting in a robust metallurgical bond. Furthermore, the presence of Y elements in the molten pool led to their attachment to the surface of un-melted W powder due to Marangoni convection. It caused abnormal diffusion of Y elements towards the pure W side of the interface. The Y element reduced the proportion of large-angle grain boundaries (LAGBs) of W close to the interface, from 36.44% to 18.90%, which further inhibited the initiation and extension of cracks. And the interfacial bonding strength reached 130.42 ± 3.27 MPa. Finally, the effect of W/steel composition gradient on the bonding phenomenon could provide a reference for the composition design and regulation of the bonding effect at multi-material interfaces. The utilization of LPBF technology for fabricating W/ODS-316L multi-material structures presents an alternative viable approach for PFC preparation.

1. Introduction

The development of high-performance plasma facet materials (PFMs) constitutes one of the most pressing and formidable challenges in the realization of commercial fusion reactor materials [1,2]. Tungsten (W) stands out as a promising candidate for the plasma-facing component (PFC) in fusion reactors due to its low physical sputtering erosion yield, high melting point, exceptional thermal conductivity, and minimal retention of radioactive tritium (T) and other hydrogen isotopes from the plasma fuel [3–5]. However, pure W exhibits brittle and hard properties, rendering it unsuitable as a structural material [6,7]. Consequently, the concept of integrating PFMs with structural materials to create strongly bonded multi-materials has been proposed to expand the freedom in structural design [8].Oxide dispersion-strengthened (ODS) steel, characterized by nanoscale oxide particles homogeneously dispersed in a steel matrix, has emerged as a reference structural material for fusion nuclear reactors, thanks to its outstanding high-temperature mechanical properties, corrosion resistance, and resilience to irradiation swelling [9,10]. Therefore, the key to enhancing the potential of W in PFC-related applications lies in the design and fabrication of W/ODS steel multi-materials that possess a high-strength and high-precision joint at the interface between W and ODS steel.

* Corresponding authors.
E-mail addresses: yanzhou@hust.edu.cn (Y. Zhou), cheys@zzu.edu.cn (Y. Che).

https://doi.org/10.1016/j.matchar.2024.114242
Received 21 October 2023; Received in revised form 15 July 2024; Accepted 3 August 2024
Available online 5 August 2024

A multi-material component comprises multiple materials distributed within a single part, allowing the integration of structures and functions to achieve customizable properties (e.g., local wear resistance, high thermal conductivity, thermal insulation, chemical corrosion resistance) at predefined locations within the component [11]. Traditionally, the creation of multi-material components from two or more dissimilar metals is typically achieved through processes like diffusion bonding [12,13], brazing [14], friction stir welding [15], and explosion welding [16], among others. Nevertheless, these conventional bonding techniques encounter limitations when manufacturing parts with intricate geometries. For instance, explosive welding and diffusion bonding necessitate mating materials with flat and congruent surfaces. While not restricted by material shapes, brazing and other welding methods face challenges when dealing with components featuring complex internal structures, substantially restricting design flexibility for many parts that require multi-material connections [17,18].

Recently, emerging additive manufacturing (AM) technologies have provided increased design freedom for fabricating parts with complex geometries, thanks to their layer-by-layer construction capabilities [19]. Laser powder bed fusion (LPBF), a prominent method in metallic additive manufacturing, has made significant advancements in producing a variety of multi-material components, such as Cu/Fe [20–23], Ni/Cu [24], IN718/316 L [25], NiTi/Ti6Al4V [19],WC-Co/Fe [26,27] and more, establishing a robust theoretical foundation for multi-material printing. Simultaneously, there has been in-depth research on the printing of refractory metal W [28,29] and ODS steel [30,31]. Tan [28] et al. designed and experimentally optimized parameters based on theoretical calculations to produce W with a relative density of 98.50% using LPBF equipment with optimized process parameters. The formed W displayed minimal spheroidization and macro-cracking, though a small amount of micro-cracking remained present in the build direction. Hu [32] et al. investigated the effect of adding nano- and micro-sized Y_2O_3 to pure W printing and found that introducing nano-sized Y_2O_3 reduced the formation of cracks resulting from numerous low-angle distorted W grains. Zhong [30] et al. successfully fabricated dense oxide dispersion-strengthened ODS-316 L steel with different Y_2O_3 additions using LPBF technology. In general, bimetallic material systems can be categorized as homogeneous and inhomogeneous based on the compatibility of the two metallic materials, and the W/ODS steel bimetallic material system is immiscible and inhomogeneous. During the additive manufacturing of immiscible dissimilar metals, the formation of brittle intermetallic phases, induced stresses and defects in the interfacial region is inherent [33]. Zhou [34] et al. identified the presence of Fe_2W and Fe_7W_6 intermetallic compounds within the interfacial region of W/316 L multi-material joints, fabricated using the selective laser melting (SLM) process. In a related study, Wei [35] et al. observed the propagation of cracks towards the tungsten side within the interfacial zone of W/316 L multi-material structures produced via LPBF. To address these challenges, Jiang [36] et al. introduced magnetron-sputtered Y_2O_3 as a nucleating agent at the W/low activation steel interface, and found that the addition of Y_2O_3 dispersed the precipitated FeW phase more uniformly, effectively inhibiting the formation of cracks caused by the precipitation of coarse FeW phase. Wei [35] et al. investigated the W/316 L stainless steel sandwich structure using LPBF and found that the high melting energy of W caused dense liquid W to flow into small cavities, sinking into the liquid SS and ultimately embedding itself in the SS matrix, resulting in a robust metallurgical bond between W and SS at the interface. These studies shed light on the potential for printing W on ODS steel and doping Y_2O_3 into ODS steel, offering solutions to mitigate the CET and the formation of brittle intermediate phases at the interface.

In this study, W/ODS-316 L multi-material structures without obvious defects were successfully fabricated by LPBF. The multi-material interfacial bonding mechanism was established through a series of characterization tests, and the effects of Marangoni convection, keyhole and solid-state diffusion on the diffusion path of element Y were systematically investigated. The results of this study are useful for understanding the multi-material interfacial bonding mechanism, and lay a solid foundation in the development of functional plasma face materials of nuclear fusion.

2. Experimental materials and procedure

2.1. Materials

The raw powders of spherical pure W (D50 = 37.2 μm) and 316 L stainless steel (D50 = 30.9 μm) were prepared by gas atomization, as shown in Fig. 1.W powder is screened through a 500 mesh sieve before being put into use.The chemical compositions of 316 L and pure tungsten obtained by ICP experiments (Agilent ICPOES730) are shown in Tables 1 and 2, respectively. The spherical Y_2O_3 powder purity was 99.999% with average particle size of 800 nm (Zhejiang Manli Nanotechnology Co., Ltd., China). A composite powder comprising 316 L stainless steel and Y_2O_3 was synthesized through the blending process conducted in a planetary ball mill, adhering to the nominal weight ratio of 316 L-1% Y_2O_3, resulting in the formation of ODS-316 L material. The milling operation employed 316 L stainless steel balls as the grinding medium, with a ball-to-powder ratio of 2:1, and was conducted at a rotational speed of 250 rpm/min for a duration of 2 h. The impact of ball milling is illustrated in Fig. 2, demonstrating uniform Y_2O_3 adherence to the surface of the 316 L powder. ODS-316 L blocks were fabricated through LPBF utilizing the synthesized composite powders.

2.2. LPBF process

In this experiment, the SLM-Solution 125 (Germany) machine was used to fabricate the multi-material structures. For the fabrication of W and ODS-316 L multi-material structure, the forming parameters for ODS-316 L were first optimized, followed by forming W above the optimized ODS-316 L steel. The forming parameters for the ODS-316 L composite were referenced from the parameters used for 316 L formed by using the SLM-Solution 125 machine [34]. After optimization, the final parameters for ODS-316 L were determined as follows: laser power of 320 W, scanning speed of 700 mm/s, scanning spacing of 0.12 mm and layer thickness of 0.05 mm. Given the immiscibility of W and ODS-316 L, which predisposes them to pore and crack formation [33], our approach focuses on mitigating defects within the W/ODS-316 L interface by meticulously optimizing the parameters governing W formation. According to our previous study [34], the scanning space was fixedly set to 0.1 mm, the layer thickness was 0.03 mm, and the parameter combination of laser power and scanning speed for W is shown in Fig. 4a. The oxygen partial pressure of the chamber was kept below 300 ppm and the substrate is preheated to 200 °C during the LPBF process. The same *Z*-scanning strategy, i.e., interlayer rotation of 67°, was used for the formation of both W and ODS-316 L, as shown in Fig. 3a. The dimensions of both W and ODS-316 L blocks were 10 mm × 10 mm with a height of 2 mm, as shown in Fig. 3c. The dimensions of the tensile test sample and the actual tensile sample are shown in Fig. 3b and Fig. 3d, respectively.

2.3. Characterization

The formed samples were cut using an electrical discharge numerical control wire cutting machine.The density of the as-fabricated specimens was determined by both image analysis method using optical microscopy(OM) and the Archimedes method [28]. The density is measured using the Archimedes method by repeating each sample three times and taking the average, while the density is measured using the optical microscopy method by photographing the same size interface and counting the defects in the image to calculate the density. The densities calculated by the above two methods are averaged to represent the density of the sample.Subsequently, the cut samples were embedded and sequentially

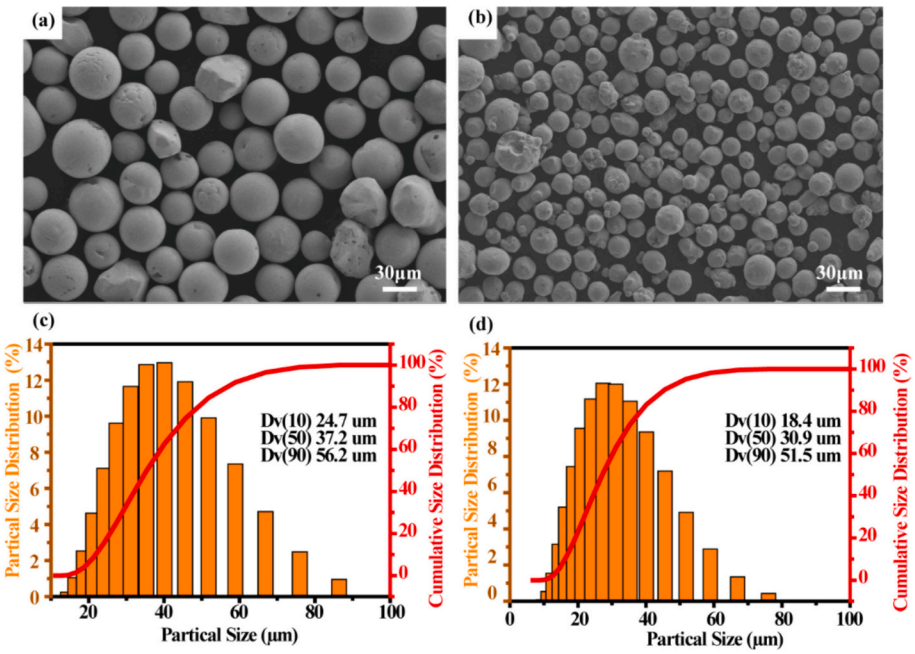

Fig. 1. Raw material powder morphology and particle size distribution: (a) SEM image of W powder and (b) 316 L powder; (c) particle size distribution of W powder and (d) 316 L powder.

Table 1
The chemical composition of the 316 L powders used in this work.

Elements	Cr	Ni	Mo	Mn	C	Si	O	S	P	Fe
(wt%)	17.45	12.55	2.24	0.08	0.023	0.91	0.03	0.01	0.02	Bal

Table 2
The chemical composition of the W powders used in this work.

Elements	W	O	C	H	N	S
(wt%)	Bal.	0.015	0.0023	<0.0005	<0.0005	<0.0005

ground on a grinder using 220, 500, and 1200 mesh diamond grinding discs, followed by polishing with 0.5 μm diamond polishing fluid and 0.25 μm alumina polishing fluid. Optical micrographs were obtained by using an Axio Imager A2m optical microscope (Zeiss, Germany). The surface morphology and element distribution of the samples were analyzed by a scanning electron microscope (SEM, Zeiss Sigma 300) equipped with an Oxford X-Max energy-dispersive X-ray spectroscopy (EDS) analyzer. The nanoindentation and elastic modulus of different regions of the interface were obtained by using a Hysitron TI 950 (Hysitron, USA). Three points of data were taken from different regions of a specimen's multi-material interface and then averaged to represent that region. The interface phases were analyzed using the Oxford STMMETRY electron backscatter diffraction (EBSD) detector, and data were obtained using AZtecCrystal analysis. After slicing and grinding the samples to a thickness of 50 μm, the samples were thinned to <100 nm using ion thinning and then characterized using a transmission electron microscope (TEM, FEI Tecnai G2 F30).Nano-indentation and elastic modulus characterization were performed using a Keysight Nano Indenter G200 (Keysight Technologies, USA). Tensile test specimens were cut using wire cutting, along the direction of multi-material block building. Tensile tests were conducted using a universal testing machine (GOTECH TCS-2000) at a rate of 1 mm/min. Three samples were tested in this direction.

3. Results

3.1. The optimization process of parameters used for W/ODS-316 L multi-material formed by LPBF

As shown in Fig. 4a, 25 multi-material samples were formed using various parameter combinations. Upon visual inspection, there were no warps, visible voids or cracks on the tungsten side of all the samples. The effect of forming parameters on the relative density of W/ODS-316 L multi-material was shown in Fig. 4(b). It is evident that a high-density region appeared in all parameter combinations, marked by the red area in Fig. 4 (corresponding to parameter combinations No. 12, No. 13, No. 18, No. 19, No. 24, and No. 25), where the densities exceeded 99%. Although this method may not provide highly precise measurements of the true density, it effectively reveals the trend of density variation with parameter changes to a certain extent.

To further investigate the influence of parameter variations on interface bonding, the interface of each sample was observed under an optical microscope (*x-z* or *y-z* plane parallel to the building direction). Fig. 5 shows the optical micrographs of W/ODS-316 L multi-material interface under different process parameters.The left side of each picture in Fig. 5 corresponds to W, and the right side of the picture corresponds to ODS-316 L.From Fig. 5, it is evident that the defects at W/ODS-316 L multi-material interface vary with the changes in process parameters. The high-density region identified in Fig. 4 is outlined with a red solid box in Fig. 5. Upon closer inspection of the interface defects within this red box, it is found that the interfaces within this region exhibit minimal or no prominent defects, mainly consisting of uniformly distributed pores. However, outside the red box, interface defects include noticeable micropores, collapsed voids, as well as cracks parallel and perpendicular to the interface. This indicates that the parameters within the high-density region of No. 12, No. 13, No. 18, No. 19, No. 24,

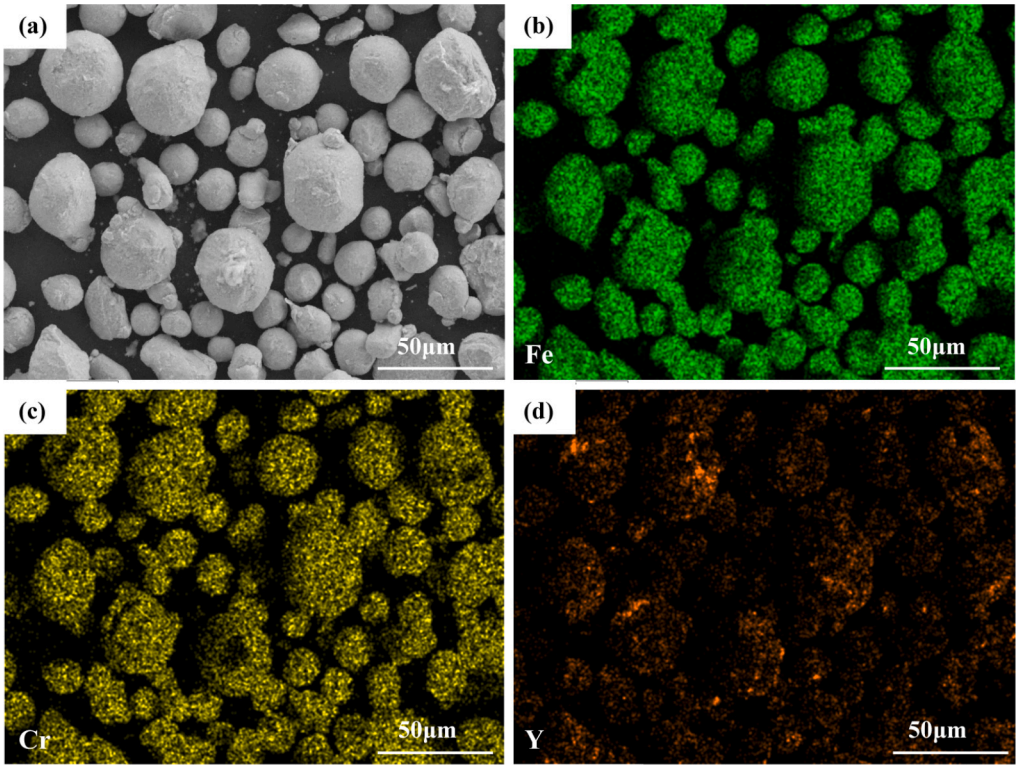

Fig. 2. Distribution of nano-Y_2O_3 on 316 L powders after ball milling process.

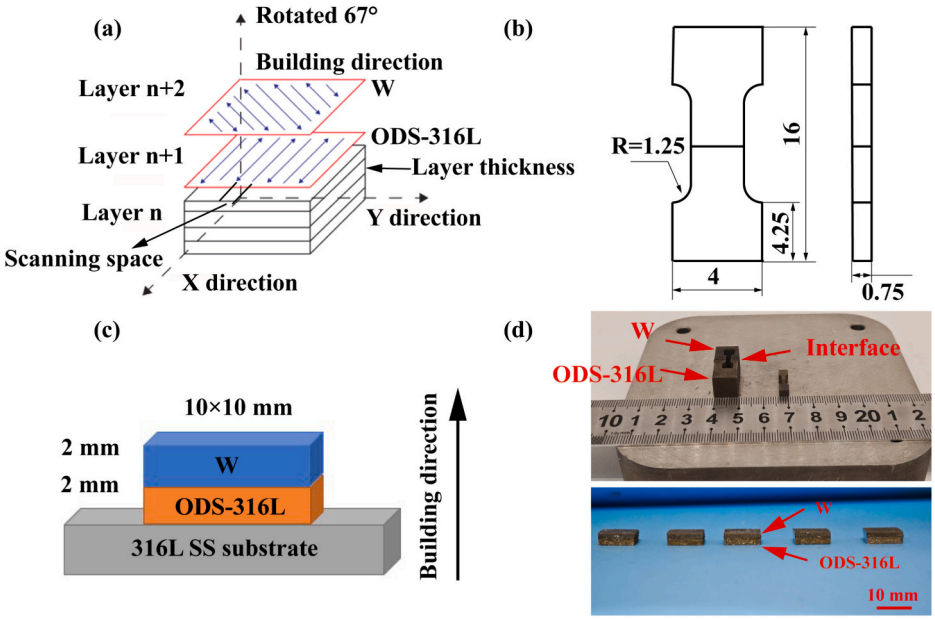

Fig. 3. (a) Scanning strategy of LPBF process; (b) dimension drawing of tensile specimens with non-standard; (c) schematic drawing of LPBF process of W/ODS steel multi-materials structure; (d) pictures of real products corresponding to (b) and (c), respectively.

and No. 25 are the most optimal among all the parameters.

In order to fully evaluate the effect of different process parameters on the multi-material bonding interface, the volumetric energy density equation [37] is introduced to provide a comprehensive measurement, which is defined as:

$$E_\nu = \frac{P}{\nu \bullet t \bullet h} \quad (1)$$

where E_ν is the laser volumetric energy input density (J/mm^3), P is the laser power (W), ν is the scanning speed (mm/s), t is the scanning spacing (mm), and h is the layer thickness (mm).

The formation of defects is closely related to the volumetric energy density variations. For instance, in the experimental sample No. 16, at a laser power of 220 W and a scanning speed of 320 mm/s, numerous incomplete melting voids and parallel cracks appeared on both sides of the interface. However, keeping the scanning speed constant, as the laser power increased from No. 16 sample with a volumetric energy density of

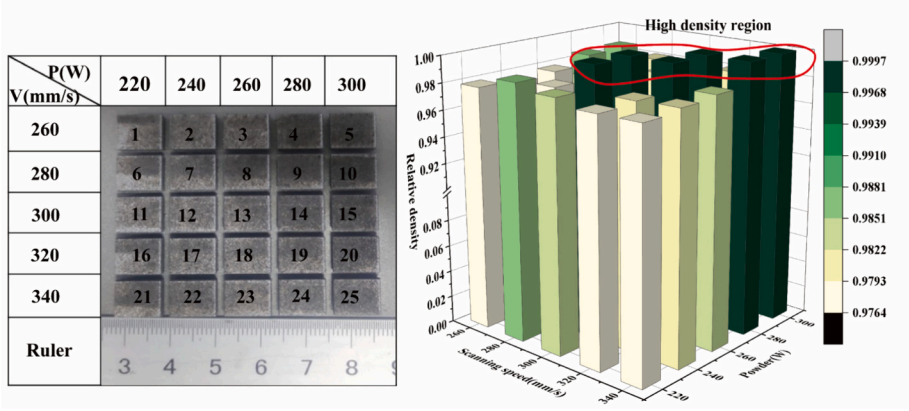

Fig. 4. (a) parameter combinations of pure W; (b) the effect of forming parameters on the relative density of W/ODS-316 L multi-material.

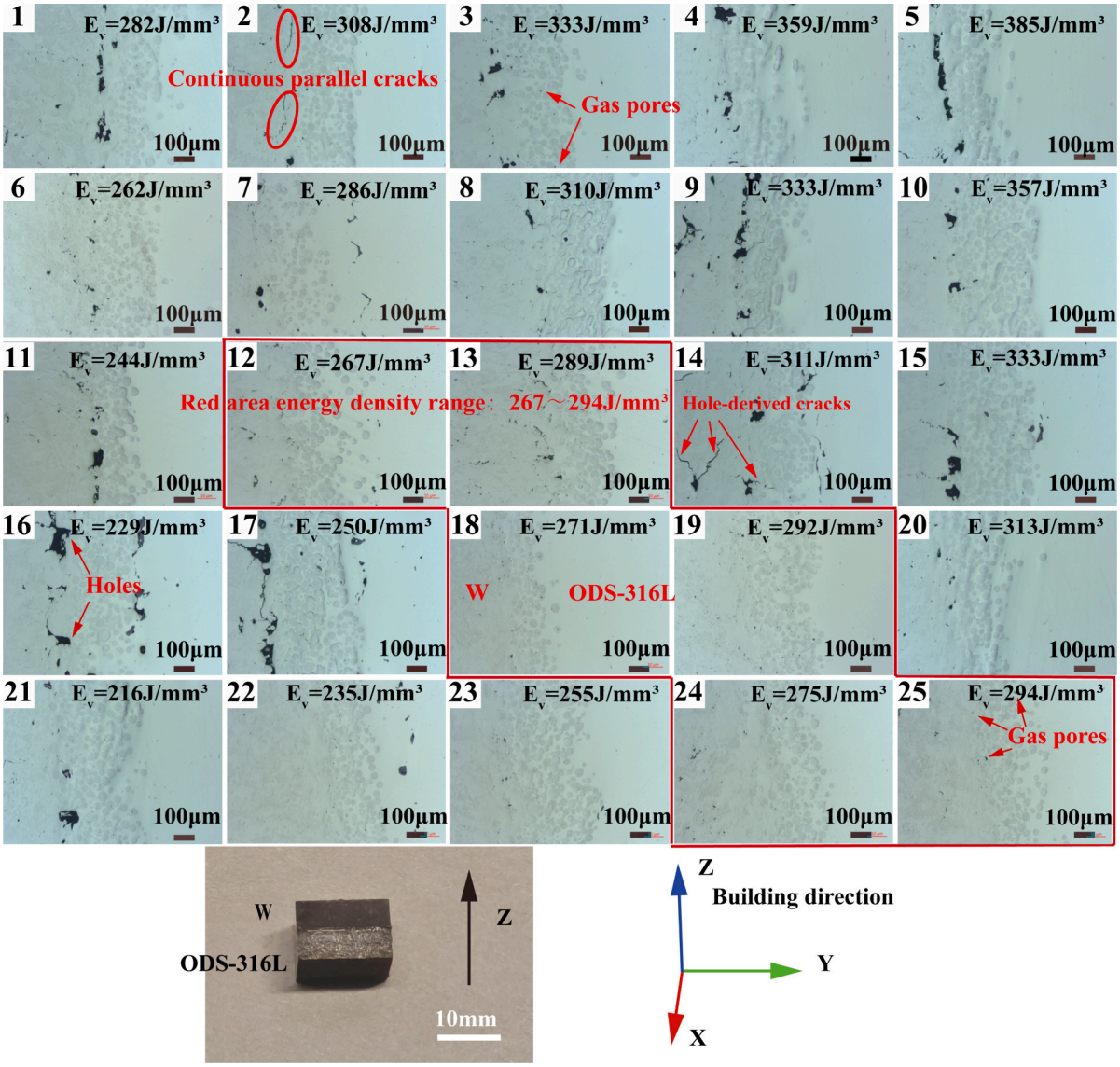

Fig. 5. Optical micrographs of W/ODS-316 L multi-material interface (W on the left and ODS-316 l on the right side of the images).

229 J/mm^3 to the No. 18 sample with a volumetric energy density of 271 J/mm^3, the incomplete melting voids and cracks at the interface disappeared, giving way to a well-bonded interface. Nevertheless, when the energy density becomes too high, as seen in the No. 14 sample with a volumetric energy density of 311 J/mm^3, excessive molten pool temperature could lead to evaporation of the pre-printed ODS-316 L,

forming keyholes [38]. Additionally, due to the small keyhole aperture, molten W, with high dynamic viscosity, fails to fill in promptly [39], resulting in the formation of collapsed voids during the solidification of the liquid metal, as demonstrated in the No. 14 sample. Moreover, during solidification with a large temperature gradient, a large amount of residual stress is gathered around the voids, so that a large number of cracks can be generated at the sharp edges of the voids, severely damaging the interface (as seen in the No. 14 sample). Furthermore, the high energy density required for forming pure tungsten results in a narrow parameter window. Even within a reasonable volumetric energy density range, the relatively low scanning speed for forming the multi-material interface with pure tungsten leads to increased molten pool depth and larger keyhole apertures [40], resulting in the formation of a series of voids parallel to the multi-material interface (as seen in samples No. 1, No. 6, No. 7). Additionally, we also considered the issue of keyhole recoil stress that may occur when re-melting pre-printed ODS-316 L at high energy densities [41], as well as the continuous parallel cracks at the connection between the multi-material interface and pure tungsten side. Therefore, considering the comprehensive analysis, the ideal parameter combination should be within the energy density range of 267 J/mm^3 to 294 J/mm^3, and the scanning speed should be >300 mm/s (as indicated in the red area in the figure). Accordingly, considering the actual situation of forming pure tungsten in this setup, the determined parameters for forming the multi-material with pure tungsten on one side are $P = 260$ W, v = 320 mm/s. The final forming parameters for W/ODS-316 L multi-materials are presented in Table 3.

3.2. The interface microstructure of W/ODS-316 L multi-material

3.2.1. Interfacial element diffusion

Though rapid solidification (10^3–10^8 K s^{-1}) [42,43]happens during LPBF process, elemental segregation, diffusion and formation of new phases remain occurring unavoidably within transient molten pool driven by thermodynamic factors. To reveal the element distribution of W/ODS-316 L bonding interface, an SEM image (Fig. 6a) of representative region with an area size of 800 μm × 600 μm (*x*-*z* plane) was used to analyze the matrix element distribution of W, Fe and the doping element of Y by EDS mapping. According to Fig. 6a, nearly unmolten pure W powder particles were found to loosely distribute at the front outer edge of the initial printed several layers of pure tungsten and penetrated into the iron matrix, occupying approximately 300 μm length along the *z* direction. The density of powder piling up showed an increase trend along the building direction. Fig. 6b-6d showed the distribution of Fe, W and Y, respectively, where an interesting phenomenon of abundant Y element diffusing and transferring from original solidified iron matrix to following as-fabricated tungsten matrix was observed as depicted by Fig. 6d. To further explain this, EDS line scanning (Fig. 6e) with a scanning line length of 400 μm was conducted in Fig. 6a as marked with a yellow line, and the line went through three distinct regions, which were W matrix layer (named as Region "I"), W/ODS-316 L bonding interface (named as Region "II"), and ODS-316 L matrix layer (named as Region "III"), respectively. Based on the significant change in Fe content, the thickness of Region II can be estimated by the distance between line 'P1' and 'P4', which was measured approximately 240 μm. Metallurgical bonding was found at the interface of as-fabricated W/ODS-316 L because the typical metallurgical diffusion zone was detected according to the appearance of Cr near line 'P1' within Region I, which was mainly attributed to 'Marangoni' convection occurring at re-melted micro-molten pools [23]. Furthermore, the content curve of Y supported the result of EDS mapping as an unexpected diffusion phenomenon of Y element segregating and accumulating on the surface of W powder particles and few Y could be detected at iron matrix.

Upon further observation at the interface, it was noticed that there was a sinking layer of W (indicated by the red dashed ellipse in Fig. 7(a)) in Region II, near the side of Region I, with a width of approximately 100 μm and a height of about two layers of deposited W (around 60 μm). It was evident that the submerged W layer was mixed with some un-melted W powders, and only a small amount of ODS-316 L matrix was distributed above this submerged layer. This phenomenon is likely caused by the fact that the ODS-316 L near the multi-material interface was mostly covered by W, and only a small amount of ODS-316 L was re-melted and floated up during subsequent high-energy-density W printing when several layers of W were printed on the already formed ODS-316 L. Furthermore, tungsten diffusion into the re-melted ODS-316 L was observed in Region II, near the side of Region III. To investigate this diffusion phenomenon, a magnified observation of the region within the red dashed box in Fig. 7(a) was performed to obtain Fig. 7(b). Combining its EDS maps (Fig. 7(c)-(g)), it was evident that the diffused W element was distributed around the un-melted W powders, diffusing towards the re-melted ODS-316 L matrix in a 'smoky' diffusion manner [44].

As described before, an abnormal phenomenon that the un-melted tungsten powders found in Region II and the tungsten layer in Region I (indicated by the black dashed box in Fig. 6e and Fig. 7g, respectively) exhibited higher Y element content compared to Region II with re-melted ODS-316 L matrix and ODS-316 L matrix in Region III. In this study, where element Y was added only to the 316 L stainless steel powder, the theoretical concentration of element Y at the interface is expected to decrease in a gradient from the ODS-316 L matrix to the W matrix, according to the diffusion of the element concentration from high to low. However, the actual concentration of Y was found to be contrary to the expected concentration gradient. The influence of this abnormal diffusion on the multi-material interface will be further explored in discussion.

3.2.2. Phase analysis

Our previous work has identified that W/316 L multi-material interfaces spontaneously produced μ-Fe_7W_6 and λ-Fe_2W intermetallic compound phases during LPBF process [34]. Though the addition of Y_2O_3 plays scant role in reaction with tungsten matrix or iron matrix due to its thermodynamic stability, the ultra-high temperature of LPBF may provide Y_2O_3 with atomic driving force to cause lattice distortion and introduce solid solution atoms to produce new solid solution strengthening phases. Fig. 8 shows the TEM results for the LPBF-fabricated W/ODS-316 L multi-material interfaces. SEM image (Fig. 8a) showed that obvious Y_2O_3 nanoprecipitations diffusely distributed in matrix. In the bright-field image (Fig. 8b), high-density dislocation tangles and uniformly distributed nano-precipitates were observed, and dislocation tangles were concentrated around nano-precipitates. The size of gray–white nanoprecipitates were further measured to be approximately 50 nm to 100 nm. EDS results (Fig. 8c and Fig. 8d) indicated the gray–white precipitate (marked by a red dotted circle) was turned out to be a Y- and O-rich nanoprecipitate. The selected area electron diffraction (SAED) pattern (Fig. 8e) identified it as the Y_2O_3 phase with a polycrystalline structure. Therefore, Y_2O_3 was considered to be partly or entirely melted under ultra-high temperature of LPBF with its particle size reduced from 800 nm to 50-100 nm. Moreover, the edges and centers of Y_2O_3 nanoprecipitates exhibited different colors, and there were differences in elemental distribution (indicated by the red dashed circle in Fig. 8d), suggesting the presence of other phases at the edges of these nanoprecipitates. FFT (Fast Fourier Transform) and inverse FFT transformations of the high-resolution TEM (HRTEM) images were further used to determine the lattice spacing of selected edge region (indicated

Table 3
The forming parameters of W/ODS-316 L multi-material fabricated by LPBF.

Forming parameters	ODS-316 L	W
Laser power (W)	320	260
Scanning speed (mm/s)	700	320
Scanning space (mm)	0.12	0.1
Layer thickness (μm)	50	30

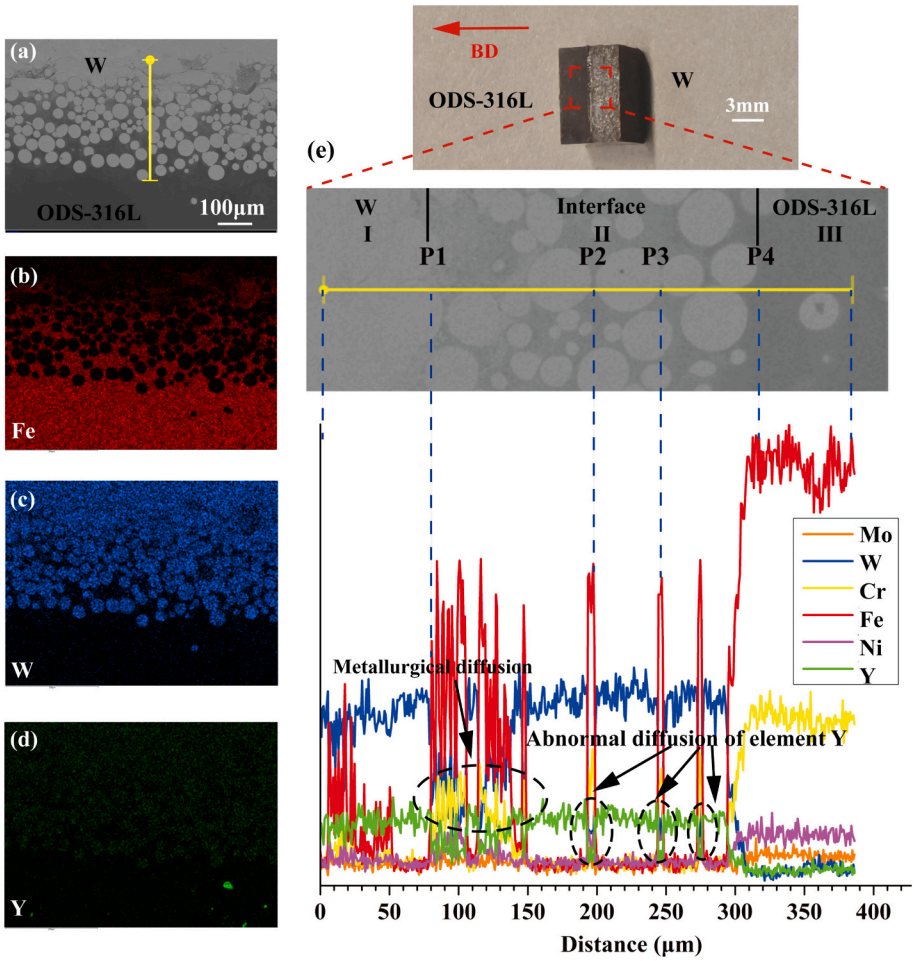

Fig. 6. SEM images and EDS results of W/ODS-316 L interfaces: (a) representative SEM micrograph of W/ODS-316 L multi-material interfaces; (b)-(d) EDS maps for Fe, W and Y; (e) element content change curve of Mo, W, Cr, Fe, Ni and Y acquired by EDS in Fig. 6a.

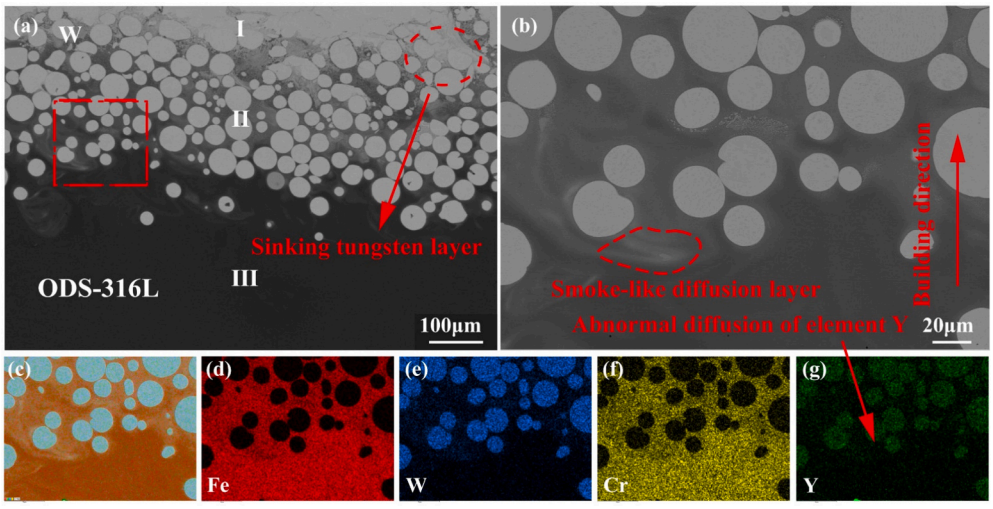

Fig. 7. SEM and BSE images of the multi-material interface under different resolutions and corresponding EDS mappings.

by the yellow frame in Fig. 8f), which was measured to be 2.11 Å, corresponding to the (−202) crystal plane of $Y_2Si_2O_7$. During solidification Y^{3+} ions were generated from the decomposed Y_2O_3 nanoparticles in Fe-based alloys with low solubility [45]. The accumulated Y^{3+} ions were uniformly dispersed in the matrix. Y_2O_3 consists of two parts, one part of un-melted or partially melted Y_2O_3 nanoparticles and one part of Y_2O_3 generated by the reaction of Y^{3+} [46]. The incorporation of a minor Y element content facilitates the dispersion and distribution of Si within the material matrix [45]. Consequently, the residual Y^{3+} ions are polarised with Si oxides to form Si-Y-O particle shells in the incipient Y_2O_3 [47].Hence, the W/ODS-316 L multi-material interfacial bonding strength might be enhanced based on high-density dislocation

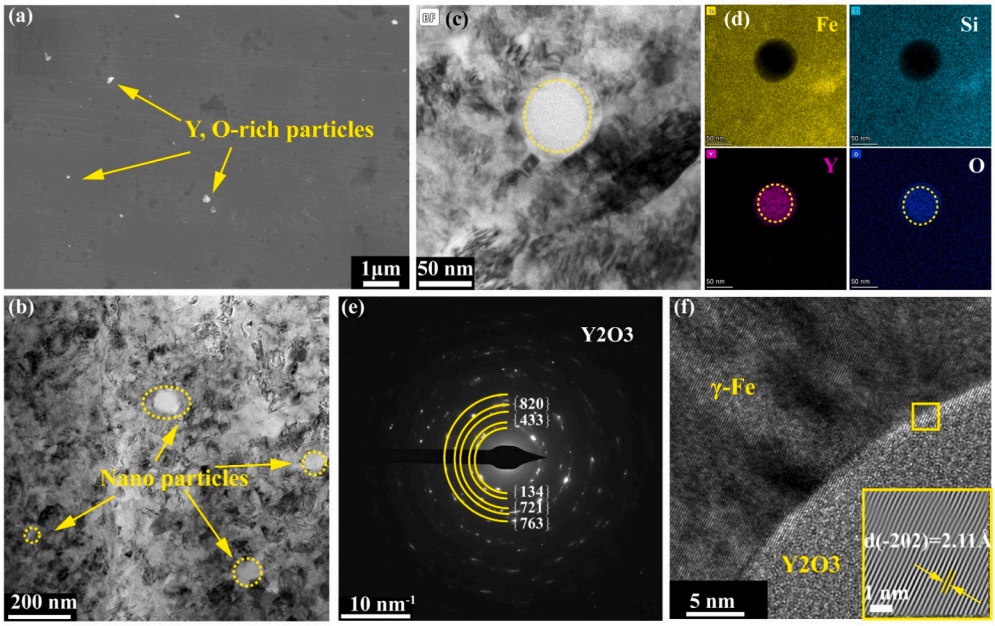

Fig. 8. TEM and EDS mapping images of nanoprecipitates and phases: (a) SEM of selected W/ODS-316 L interfacial region; (b) and (c) bright-field images; (d) EDS mapping images (e) SAED pattern of nanoprecipitates; (f) HRTEM image of nanoprecipitates and the inset image shows the IFFT in corresponding region.

strengthening originated from solid solution $Y_2Si_2O_7$ phase and oxide dispersion strengthening of Y_2O_3 nanoprecipitates.

3.3. *Interfacial nano-hardness and elastic-modulus of W/ODS-316 L multi-materials*

To reveal the distribution of nano-hardness and elastic modulus of W/ODS-316 L multi-material interfaces, nanoindentation testing was carried out on the *x-z* plane where five representative regions have been defined for better comparation and analysis. The region where unmelted W powder and molten ODS-316 L are blended at the multi-material interface, spanning approximately 500 μm in width, is defined as the W → ODS-316 L interface. Adjacent to the W → ODS-316 L interface on both sides, there are regions with an approximate width of 200 μm where elements can diffuse; these are defined as W near the interface and ODS-316 L near the interface, respectively. In regions distant from the W → ODS-316 L interface, where element diffusion is not observed, a 500 μm-wide area is chosen for W, defined as W-top, and a 500 μm-wide area is selected for ODS-316 L, defined as ODS-316 L bottom. For each region, three measurement points were selected and the obtained values were averaged to represent the final nano-hardness and elastic modulus values for each particular region, as illustrated in

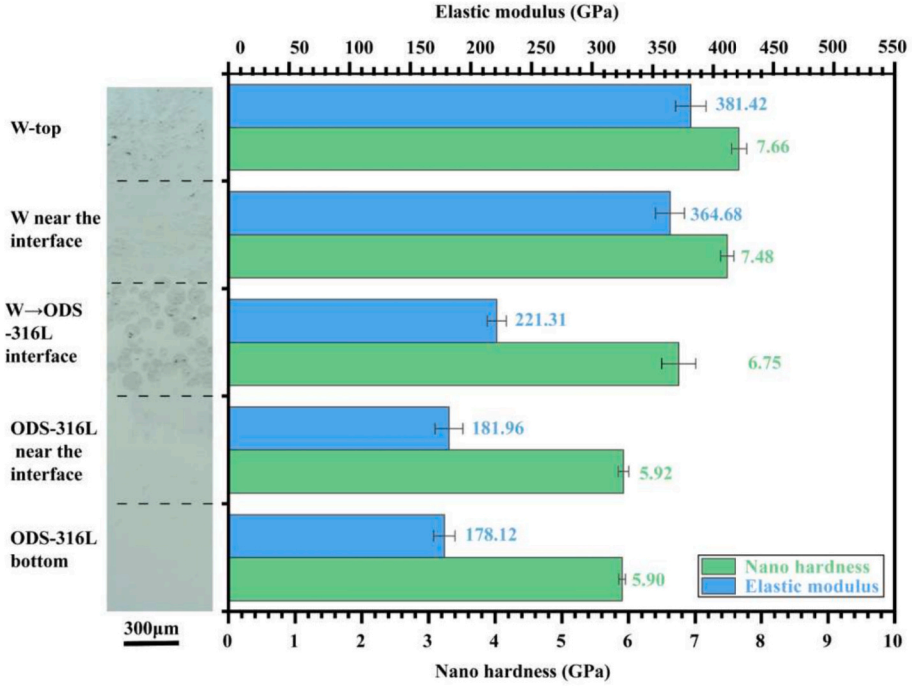

Fig. 9. Nano-hardness and elastic modulus of different regions in W/ODS-316 L multi-material interface.

Fig. 9. The moderate nanoindentation hardness of 6.75 ± 0.34GPa at the multi-material interface which fell into the range of W matrix (7.66 ± 0.12 GPa) and ODS-316 L matrix (5.90 ± 0.08 GPa). The distribution of elastic modulus resembled nano-hardness and the elastic modulus of W → ODS-316 L interface (221.31 ± 7.93 GPa) also fell between the values of W matrix (381.42 ± 12.65 GPa) and ODS-316 L matrix (178.12 ± 8.91 GPa). The brittle Fe—W intermediate phase nano-hardness is higher than the nano-hardness of W and ODS-316 L. The above nano-hardness data, on the other hand, indicate that the brittle Fe—W intermediate phase does not exist at the interface of the various materials. The intermediate values of nanoindentation hardness and elastic modulus can be attributed to its combination of higher nano-hardness of W and lower elastic modulus of ODS-316 L [35].

3.4. Tensile properties and fracture morphology of W/ODS-316 L multi-materials

The direct fabrication of W/ODS-316 L composite tensile specimens using conventional methods is notably challenging, leading to limited reports on their tensile properties. Fig. 10 illustrates the tensile stress-strain curves of W/ODS-316 L and W/316 L multi-materials. Prior to fracture, all stress-strain curves followed approximately linear elastic fracture characteristics with an elongation of 0.36 ± 0.03%, indicating a typical brittle fracture mode. The tensile strength of W/ODS-316 L specimen reached 130.42 ± 3.27 MPa, which represents a significant improvement compared to W/316 L multi-material(96.67 ± 2.36 MPa). This implied that the addition of Y_2O_3 improved the interfacial strength. However, the ultimate tensile strength of the W/ODS-316 L specimens remained noticeably lower than that of ODS-316 L material [30]. This suggests that the limiting factor for enhancing the strength of W/ODS-316 L lies not in tungsten itself but the quality of the interface bonding.

The TEM data presented earlier indicate the absence of any significant Fe—W intermediate phase at the interface, or at most, the presence of such phase in trace amounts that are difficult to detect. As a result, interface strength is largely governed by the defects present therein. To characterize this further, we selected one fractured specimen, and the fracture morphologies are depicted in Fig. 11. Fig. 11a and e illustrate the fracture surfaces of ODS-316 L and tungsten, respectively. From Fig. 11a, it was evident that pores and un-melted W powders were distributed throughout the fracture surface, with the size of some pores even reaching approximately 50 μm (as seen in Fig. 11b). According to the magnified images (Fig. 11c and d) corresponding to the white dashed boxes B and C in Fig. 11a, cleavage steps and carbide/nitride impurities were observed, respectively. Cleavage steps are considered the feature of brittle fracture [48], while carbide/nitride impurities tend

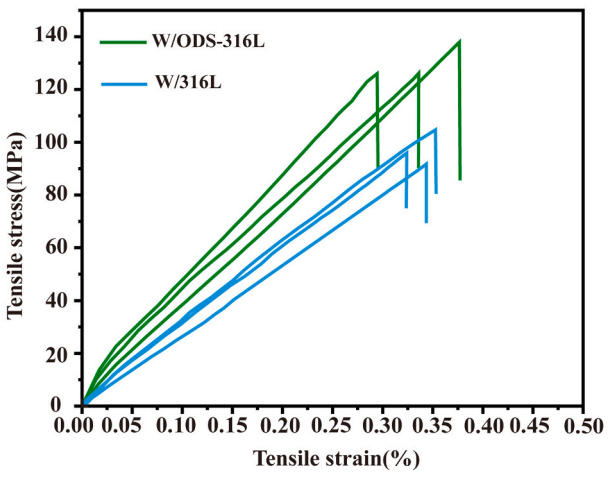

Fig. 10. Tensile stress-strain curves for W/ODS-316 L and W/316 L multi-material samples.

to act as stress concentration sites during deforming, leading to premature fracture initiation and a significant reduction in yield strength. The fracture morphology of W matrix (Fig. 11e) was similar to that of ODS-316 L and there were more un-melted tungsten powders. Importantly, numerous cracks were observed on this fracture surface. Fig. 11f presents a close-up view of the white dashed box D in Fig. 11e, revealing that cracks initiated at the interfaces between the un-melted W particles and the matrix and further propagated into the matrix.

Hence, the primary factors influencing interfacial fracture failure encompass both interfacial defects and the presence of un-melted W powder at the interface, elucidated through the specific mechanism depicted in Fig. 11g. Despite parameter optimization efforts, the immiscibility of W and ODS-316 L persists, resulting in residual pores and microcracks at the interface. Under external loading, the weakening bond between un-melted W powder and ODS-316 L gradually deteriorates, while concurrently, microcracks surrounding the un-melted W powder and carbon/nitrogen compounds undergo rapid expansion towards the ODS-316 L matrix, ultimately culminating in diminished bonding strength at the W/ODS-316 L interface.

4. Discussion

4.1. Elemental diffusion analysis

There are compositional differences at the interface of heterogeneous materials, and the sharp difference in composition promotes intense diffusion of atoms at the interface. Printing high melting point tungsten on the printed ODS-316 L materials is equivalent to introducing tungsten element existing as raw tungsten powder particles in region II (as described in Fig. 6) to the interface, which means that intense diffusion of atoms occurs at the W/ODS-316 L multi-material interface. From Fig. 6b, it can be seen that the diameter of the un-melted tungsten powder is small, and the diffusion distance of 240 μm has exceeded the diameter of the tungsten powder, so the diffusion appearing at the multi-material interface can be explained by the unsteady state diffusion in solid state diffusion (SSD) [35,49]. Based on Fick's second law, change rate of concentration is the product of the diffusion coefficient and the second-order differential of the concentration gradient, as shown in Eq. (2):

$$\frac{\partial_\rho}{\partial_t} = \mathrm{D}\left(\frac{\partial_\rho^2}{\partial x^2} + \frac{\partial_\rho^2}{\partial y^2} + \frac{\partial_\rho^2}{\partial z^2}\right) \tag{2}$$

Where ρ is the mass concentration of the diffusing substance, t is the time, D is the diffusion coefficient, x, y, z represent the direction of diffusion in three-dimensional space, and $\frac{\partial_\rho^2}{\partial x^2}$、$\frac{\partial_\rho^2}{\partial y^2}$、$\frac{\partial_\rho^2}{\partial z^2}$represent the second-order differentiation of the concentration gradient.

The diffusion coefficient D is a function of temperature and molar atomic diffusion activation energy and its expression is shown in Eq. (3):

$$D = \mathrm{D}_0 exp\left(-\frac{\mathrm{Q}}{\mathrm{R}T}\right) \tag{3}$$

where D_0 is the diffusion constant, Q is the diffusion activation energy, and T is the absolute temperature, R is the universal gas constant. The main factors affecting this diffusion are temperature and concentration gradient as shown by eqs. (2) and (3). When printing a multi-material structure, heat conducts downward from the print layer and the constant flow of heat keeps the temperature of the interface at a high level. The diffusion activation energy of different elements determines the rate of elemental diffusion. The higher the temperature, the more violent the motion of the atoms, the more likely they are to jump and the higher the diffusion coefficient. The heterogeneous material mixing of the multi-material at the interface provides a sharp concentration gradient. The sharp concentration gradient of each element at the multi-material interface intensifies the solid-state diffusion at the multi-material

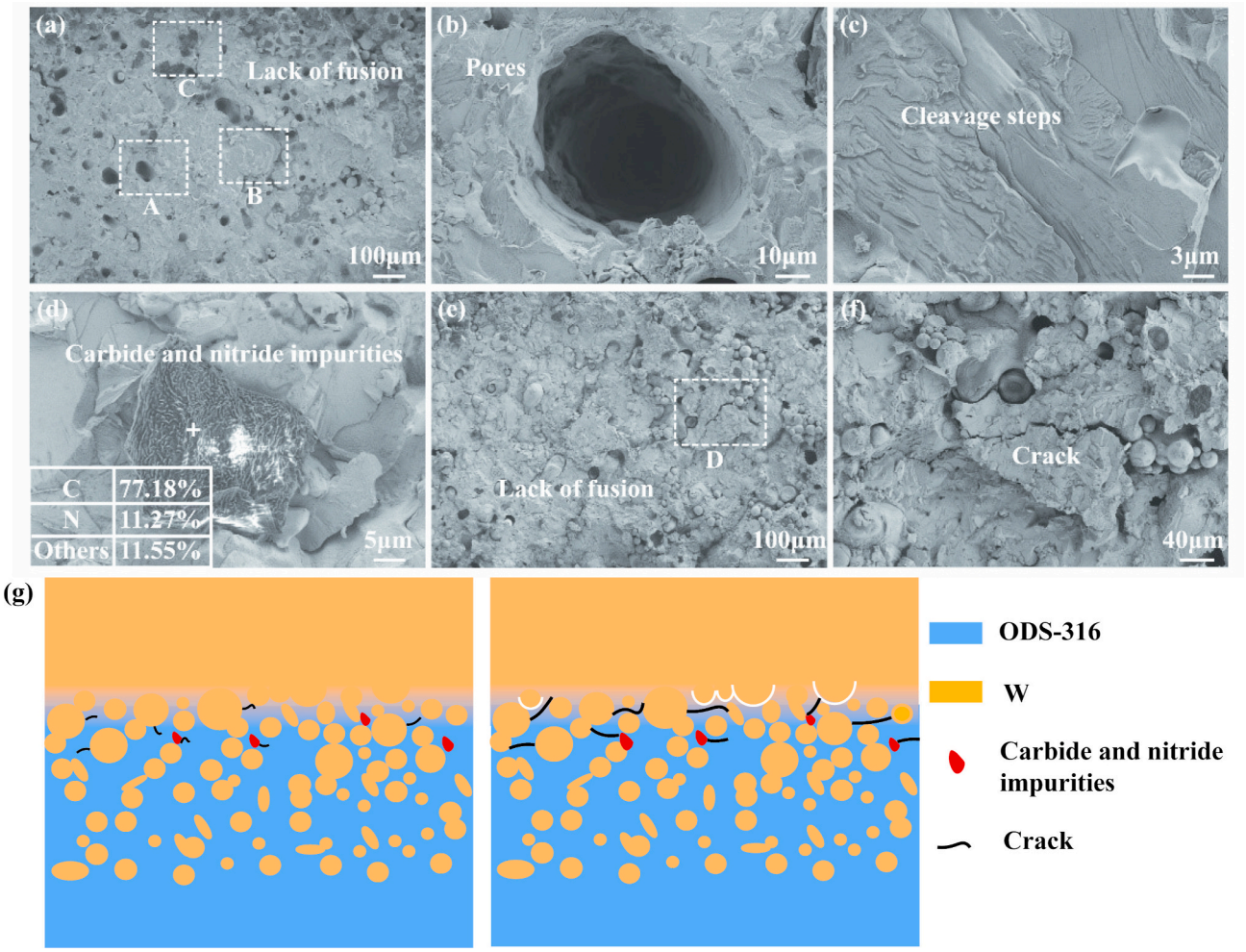

Fig. 11. Fracture morphologies of W/ODS-316 L tensile sample: (a) entire ODS-316 L fracture; (b)-(d) high magnification SEM images corresponding to regions A, B, and C in Fig. 11(a), respectively; (e) entire W fracture; (f) high magnification SEM image corresponding to region D in Fig. 11(e) ; (g) Interface failure mechanism.

interface during the LPBF process. As a result, the combination of the increased diffusion coefficient and the drastically changing concentration at the multi-material interface results in an increased diffusion rate of the elements at the multi-material interface, which results in a good metallurgical bond.

However, it has been observed that the actual diffusion behavior of W element at the multi-material interface does not completely conform to the description of Fick's second law, as the diffusion of W element does not exhibit a gradient distribution from tungsten matrix to ODS-316 L matrix. Instead, the diffusion paths and morphologies of W element at the multi-material interface resemble the circulation pattern observed during molten pool 'Marangoni' convection. It is explained that the bottom bulk ODS-316 L enhances the dissipation of heat from the molten pool, leading to increased temperature and surface tension gradients between the center and edge of the molten pool, thereby enhancing the dynamics of 'Marangoni' convection, resulting in the formation of circulation patterns at the interface of the molten pool [50]. As a consequence, un-melted W powder is entrained into the circulation and moves with the flow while being subjected to the high temperature of the molten pool, providing the diffusion activation energy for W powder surface elements to diffuse towards ODS-316 L. In summary, the entrained W powders experienced surface melting under the high temperature conditions of the molten pool, and the diffusion of W element was governed by the combined effects of Fick's second law and Marangoni convection. During this stage, the diffusing W element underwent circular motion within the molten pool [50], driven by 'Marangoni' convection. The final diffusion results, as depicted in Fig. 8, show that W element assume a smoky appearance and are distributed around the tungsten powder without significant concentration gradients at the interface with ODS-316 L.

Regarding the abnormal diffusion of Y element at interfaces, it is closely related to the dynamic melt pool during molding of multi-material interfaces. During LPBF process, the melt pool was subject to complex dynamic melt flow conditions such as gravity, buoyancy, recoil stress and Marangoni convection during multi-material interface molding due to the vastly different physical properties of the two materials [51–53]. Considering that the mass of Y_2O_3 nanoparticles is too small, its gravity and buoyancy are neglected and it flows with the flow of the molten pool [54]. Nanoparticles dispersed in the melt pool show strong tendencies towards agglomeration and aggregation due to their high surface area, high interfacial energy with the surrounding metallic melt and van der Waals forces [55,56]. As a result, Y_2O_3 in re-melted ODS-316 L was 'adsorbs' on the un-melted tungsten powder as it moves in the dynamic melt pool during the forming of the W/ODS-316 L multi-material interface.

4.2. Influence of abnormal distribution of Y elements on W/ODS-316 L multi-material interface

As shown in Fig. 13, EBSD results of W/ODS-316 L multi-material interface was obtained including grain orientation and size distribution, texture intensity, kernel average misorientation (KAM), grain

boundary misorientation distribution (GBMD) to illustrate the detailed effect of Y abnormal elemental diffusion on microstructural evolution and mechanical properties. It should be noted that there were a few regions of physical phase type which could not be identified at the multi-material interface, and the unidentifiable regions were shown as black. According to BD-IPF images (Fig. 12a), the basically random distribution of color indicated that there was no preferred orientation of grain growth, and the maximum texture index was calculated to be only 4.72 (Fig. 12d). Furthermore, a microstructure consisting of abundant ⟨110⟩ and ⟨111⟩ oriented elongated columnar grains among ODS-316 L matrix was obtained while a dominantcoarse grains with a strong ⟨111⟩ orientation could be found in W matrix. It was noteworthy that there were some fine equiaxed grain regions (as marked by white dash box) occurred near the interface of W/ODS-316 L after LPBF process. Fig. 12e and f show the grain size distribution of W/ODS-316 L interfacial region and single ODS-316 L matrix region. The average grain diameter of W/ODS-316 L interfacial region was 2.55 ± 0.06 μm, which was greatly smaller than the average grain diameter of single ODS-316 L matrix region (15.88 ± 0.13 μm). Even though both experience supercooling during rapid solidification of LPBF and the Y_2O_3 nanoprecipitates and solid solution $Y_2Si_2O_7$ phases providing more heterogeneous nucleation sites [57], the average grain sizes still differ significantly. On the one hand, the Y concentration difference in the W/ODS-316 L interface region accompanied by the diffusion of Cr and tritiated Si (as described in the previous section) increases the degree of compositional supercooling at the W/ODS-316 L interface, and the grain growth changes to an equiaxed grain mode [58,59]; on the other hand, the W/ODS-316 L interface is divided into several small regions by the presence of un-melted tungsten powders, and the surface of the un-melted tungsten powder served as heterogeneous nucleation site to refine the grains in this region. Hence, a large amount of grains nucleated at the interface and failed to grow larger, resulting in dominant fine equiaxed grain regions.

Figure 12(b) shows the KAM map corresponding to Fig. 12(a), where KAM value is defined as the average orientation difference between each measured point and the nearest neighboring point (orientation differences of >5° excluded from the calculation). KAM value can be used to characterize local plastic strain, and thus, dislocation density can be roughly described by the KAM map. Region A and B were defined as the transition region from central interface to ODS-316 L matrix and the transition region from central interface to W matrix, respectively. The KAM value of Region A was obviously higher than that of Region B which indicated a higher dislocation density caused by hinder effect of fine grain boundaries. Furthermore, the distribution of high KAM value

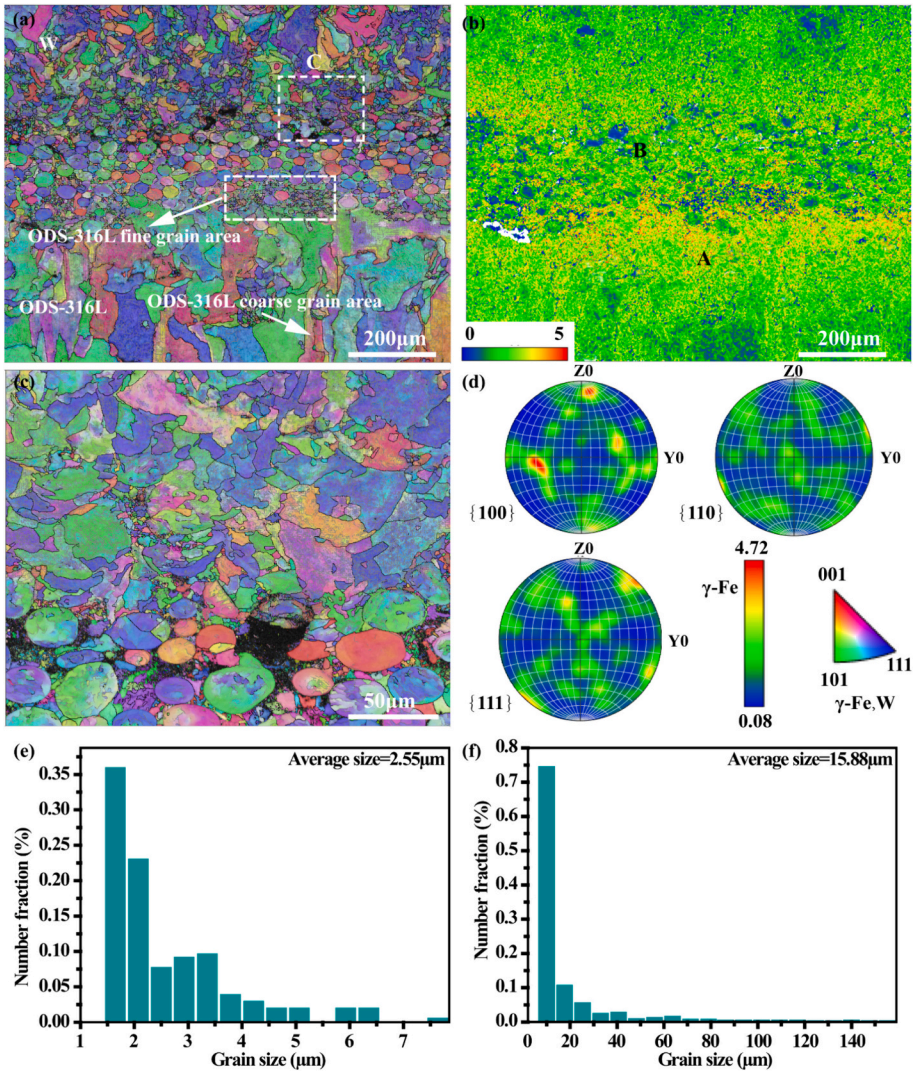

Fig. 12. Interfacial EBSD analysis of W/ODS-316 L multi-materials:(a) BC + IPF + GB; (b) KAM map; (c) high resolution image of BC + IPF + GB corresponding to the region marked by white dashed box in Figure a; (d) PFs; (e) and (f) distribution histogram of average grain size corresponding to fine grain region of ODS-316 L at the interface and coarse grain region on ODS-316 L matrix, respectively.

in Region A was found to appear at the micro-cracks. In general, higher stress concentration means a weaker performance area, and Region A may become the initial failure when deformation occurs. For Region B, W matrix has a high ductile-brittle transition temperature (DBTT), and is more susceptible to stress concentration and microcrack formation during cooling [60]. The large difference between the coefficients of thermal expansion (CTE) of W and 316 L also facilitates cracking.

Figure 13 shows the microstructural misorientation angle distribution of as LPBF-fabricated W/ODS-316 L multi-materials along the building direction. Fig. 13a and c illustrated the distribution of low-angle grain boundaries (LABGs) and high-angle grain boundaries (HABGs) in W matrix region which was far from interfacial bonding region and had few Y diffusion and W/ODS-316 L interfacial region, respectively. Here, LAGBs) were defined with a misorientation of 2°–15°, while HAGBs were defined with a misorientation of >15°. From Fig. 13a, in the region of the W matrix away from the interface, the proportion of HAGBs is larger and basically distributed near the coarse cracks, which are expanding along the grain boundaries. On the contrary, in the W matrix near the interfacial bonding region, the proportion of HAGBs decreases significantly, and only a very small number of microcracks are distributed. The distribution histograms of grain boundary misorientation (ranging from 2° to 60°) corresponding to above two regions were obtained, as shown in Fig. 13b and d, respectively. It was found that the proportion of HAGBs in the W region which was far away from the interface, was calculated to be 36.44%, which was almost twice the proportion of HAGBs in Region B. This implies that the Y elemental segregation reduced the proportion of HAGBs in the W matrix. LAGBs are effective in preventing crack propagation because they have zigzag grain boundaries, while for HAGBs, it is more necessary to coordinate the deformation between neighboring grains. Therefore, less dislocation accumulation and stress concentration will occur in Region B, means a higher anti-cracks capability and ultimately, a better mechanical properties performance than single W matrix.

4.3. Interface bonding mechanism

On the basis of the experimental results mentioned above, we proposed the interfacial bonding mechanism for W/ODS-316 L multi-materials. Specifically, the mechanism exhibited three different stages.

The first stage was defined happening when printing the first and second layer of W powders on the solidification surface of as-printed ODS-316 L counterpart where there was a dominant interaction of 'Keyhole' mode. Due to lower boiling point of elements in pre-printed ODS-316 L substrate compared to the melting point of W powder, the high energy density input during the formation of the first two W powder layers resulted in the formation of a keyhole at the interface [38]. Evaporation of elements from pre-printed ODS-316 L generated recoil stress that separated the molten pool, causing direct function of laser energy at the bottom of the molten pool, resulting in the deepening of the molten pool and the formation of a slender keyhole cavity [61]. At this stage, W powders should melt and mix with liquid ODS-316 L matrix within the slender keyholes. However, most of the laser energy was consumed by the ODS-316 L matrix, resulting in incomplete melting of the W powders, a phenomenon that also occurs at the W/Fe [35] and W/Cu [49] interfaces. Small W powder particles under 20 μm were able to sink to the bottom of the keyholes due to gravity, leading to the observation of a few smaller W particles at deeper regions of ODS-316 L, as seen in Figs. 6 and7. Additionally, rapid solidification rate of liquid phase ODS-316 L made it challenging to fill the slender keyholes completely, resulting in irregular hole distribution at deeper regions of ODS-316 L matrix.

In the second stage (defined as when printing from the 3rd layer to 6th W layer), due to the incorporation of un-melted W powders into the re-melted ODS-316 L matrix under the influence of intense 'Marangoni' convection, the keyhole pattern found in the first stage did not occur. Nonetheless, super-high energy density input for melting W still led to the formation of a large molten pool, as shown in Fig. 14. At this point, high energy density input caused significant temperature gradients on the surface and within the molten pools, inducing strong 'Marangoni' convection [62]. W powders within the molten pool began to partially

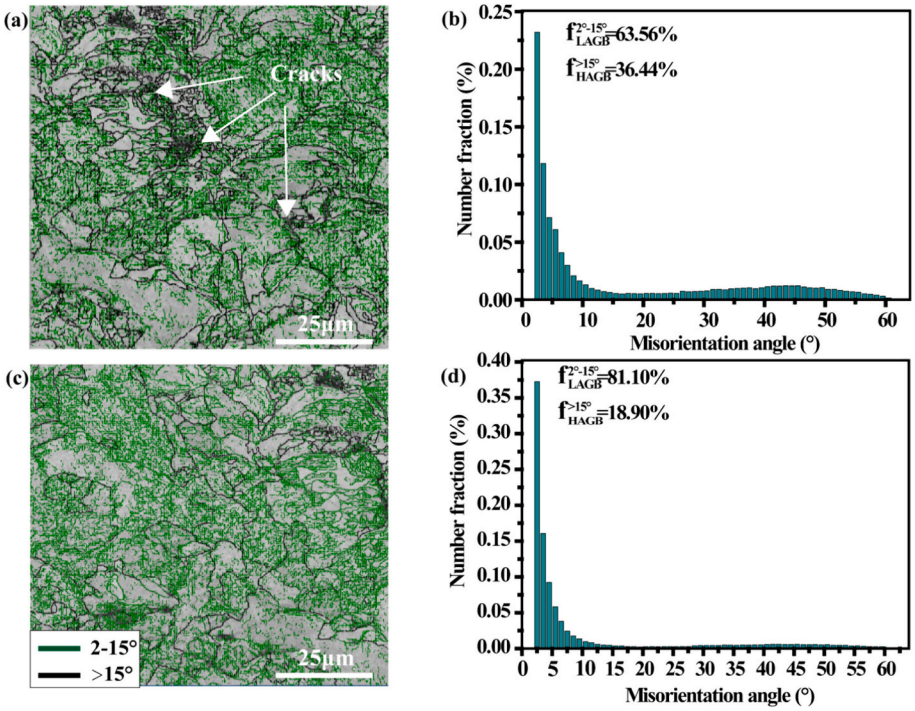

Fig. 13. (a) BC + GB image of the W region away from the interface; (c) BC + GB image corresponding to Region B in Fig. 12(b); (b) and (d) grain boundary misorientation angle distribution histograms correspond to (a) and (c), respectively.

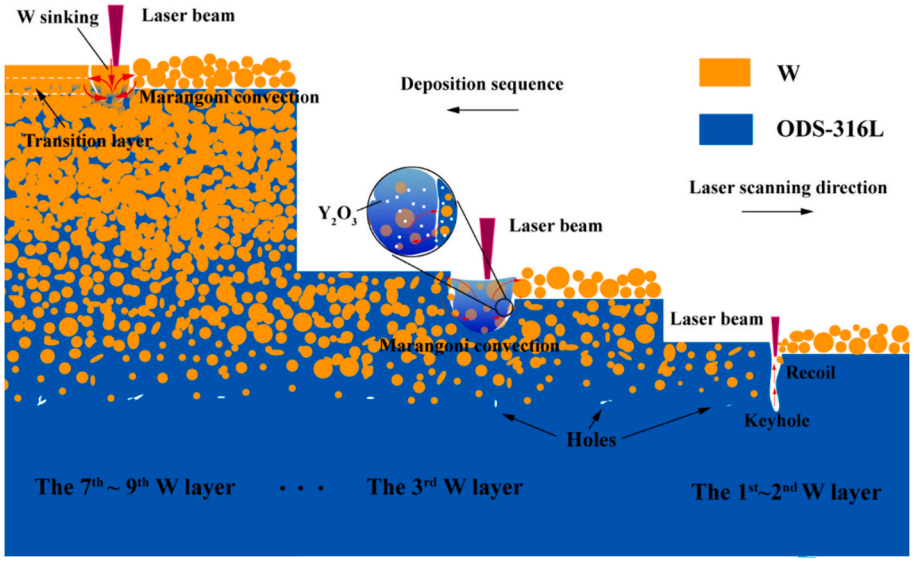

Fig. 14. Illustration of W/ODS-316 L multi-material interface bonding mechanism.

melt and diffuse into the re-melted ODS-316 L matrix under the influence of high temperature and 'Marangoni' convection, while simultaneously undergoing circular motion due to 'Marangoni' convection, as depicted in Fig. 7a. During this process, Y element diffusion took place, as illustrated in the magnified view in Fig. 14, with Y_2O_3 from the re-melted ODS-316 L continuously diffusing towards W powders due to the strong 'Marangoni' convection. This diffusion occurred throughout the interface bonding process, with particularly strong diffusion during the second stage. As the printing progresses, more and more un-melted W powders were entrained into the re-melted ODS-316 L molten pools, absorbing more energy from the laser and reducing the amount of re-melted ODS-316 L. As a result, the depth of the molten pools became shallower, leading to a gradual transition to the third stage.

In the third stage (defined as when printing the 7th layer to 9th layer), only a small amount of ODS-316 L matrix remained, and its melting consumed less energy. The majority of laser input energy was absorbed by W powders, resulting in a relatively shallower molten pool. At this stage, almost all W powders were melted, and the melted W liquid drops sank due to gravity and mixed with the previous un-melted W powders, forming a transition layer of approximately 60 μm, which is similar to that found at the W/Fe interface [35]. Furthermore, the intense 'Marangoni' convection entrained inert gas into the molten pools, and after solidification, places occupied by trapped gas formed pores, corresponding to the micro-pores observed on the W side in Fig. 3. The third stage finished after printing approximately 2 to 3 layers of W powders, at which point the interface bonding has essentially transitioned into a single W material.

In conclusion, W/ODS-316 L multi-material interface bonding mechanism is closely related to the number of W powder layers when following a printing order of W → ODS316L by LPBF. The first stage begins with a small number of W powder layers, resulting in high-energy density input that melts ODS-316 L and forms a keyhole. As more W powder layers added, the height of the multi-material interface increased and re-melted ODS-316 L decrease, the molten pool becomes shallower. By the third stage, after the formation of a transition layer of approximately 60 μm, the interface bonding has effectively transitioned into a single W material.

5. Conclusions

In this study, W/ODS-316 L multi-material components were successfully fabricated using LPBF technology. The research encompassed the examination of microscopic morphological features at the multi-material interfaces, the exploration of the influence of abnormal Y element diffusion, an investigation into the interfacial bonding mechanism, and an analysis of the bonding strength and fracture characteristics of the multi-material interfaces. The following conclusions have been drawn:

(1) By optimizing the LPBF process parameters, W/ODS-316 L multi-material samples were fabricated with a well bonded metallurgical interface. The bonding mechanism at the W/ODS-316 L interface evolved with the number of printed tungsten layers. In cases with fewer tungsten layers, a keyhole-like structure was observed. As the number of printed tungsten layers increased, a transition zone (referred to as Region II) consisting of un-melted tungsten powders and re-melted ODS-316 L emerged. The re-melted ODS-316 L underwent a transformation from columnar grains with an average size of 15.88 ± 0.13 μm to equiaxed grains with an average size of 2.55 ± 0.06 μm. This transformation was driven by compositional supercooling and the presence of nano-precipitated Y_2O_3 and $Y_2Si_2O_7$ solid-solution phases, which acted as nucleation sites.

(2) No brittle Fe—W intermediate phase was detected within the interfacial region. The nano-hardness of this region fell between that of pure tungsten and ODS-316 L, while retaining the low elastic modulus of ODS-316 L. The W/ODS-316 L multi-material exhibited a tensile strength of up to 130.42 ± 3.27 MPa, but displayed minimal ductility. The lack of ductility was attributed to the presence of numerous un-melted tungsten particles and a minor quantity of carbide and nitride impurities within the transition zone. The catastrophic failure and brittle fracture of W/ODS-316 L multi-materials were initiated by cracks and stress concentrations arising from these formation defects.

(3) The high energy density required for W caused re-melting of the pre-printed ODS-316 L, resulting in a mixed molten pool of ODS-316 L and W. Abnormal diffusion of Y element from the mixed molten pools into the adjacent transition zone reduced the proportion of HAGBs (from 36.44% to 18.90%) in W matrix. The reduction in proportion of HAGBs decreased stress concentration, improved the ductility of W and significantly reduced the number of cracks in the region.

CRediT authorship contribution statement

Zhirong Xie: Writing – review & editing, Writing – original draft,

Data curation. **Yan Zhou:** Writing – review & editing, Funding acquisition. **Xiaoqiang Wang:** Validation. **Keyu Chen:** Writing – review & editing. **Ruifang Wang:** Validation. **Shifeng Wen:** Supervision. **Yusi Che:** Validation, Methodology. **Yusheng Shi:** Validation. **Jilin He:** Validation.

Declaration of competing interest

The authors declare that they have no known competing financial interests or personal relationships that could have appeared to influence the work reported in this paper.

Data availability

The data that support the findings of this study are available from the corresponding author upon reasonable request.

Acknowledgement

This work was funded by the National Natural Science Foundation of China (No. 52274400, 52275332), National Science Fund for Outstanding Young Scholars of Hubei Province (No. 2023AFA073), and the Sixth China Association of Science and Technology Youth Talents Invitation Project (No. YESS20200326).

References

[1] J. Knaster, A. Moeslang, T. Muroga, Materials research for fusion [J], Nat. Phys. 12 (5) (2016) 424–434.
[2] Y. Wan, J. Li, Y. Liu, et al., Overview of the present progress and activities on the CFETR [J], Nucl. Fusion 57 (10) (2017).
[3] C. Ren, Z.Z. Fang, M. Koopman, et al., Methods for improving ductility of tungsten - a review [J], Int. J. Refract. Met. Hard Mater. 75 (170–83) (2018).
[4] A. Šestan, P. Jenuš, S.N. Krmpotič, et al., The role of tungsten phases formation during tungsten metal powder consolidation by FAST: implications for high-temperature applications [J], Mater. Charact. 138 (308–14) (2018).
[5] Y. Oh, N. Kwak, K. Lee, et al., Ductility enhancement of tungsten after plastic deformation [J], J. Alloys Compd. 787 (801–14) (2019).
[6] K. Li, G. Ma, L. Xing, et al., Crack suppression via in-situ oxidation in additively manufactured W-ta alloy [J], Mater. Lett. (2020) 263(.
[7] P. Rebesan, M. Bonesso, C. Gennari, et al., Tungsten fabricated by laser powder bed fusion [J], BHM Berg- und Hüttenmännische Monatshefte 166 (5) (2021) 263–269.
[8] P. Norajitra, L.V. Boccaccini, A. Gervash, et al., Development of a helium-cooled divertor: material choice and technological studies [J], J. Nucl. Mater. 367-370 (1416–21) (2007).
[9] M.E. Medhat, Y. Wang, Investigation on radiation shielding parameters of oxide dispersion strengthened steels used in high temperature nuclear reactor applications [J], Ann. Nucl. Energy 80 (365–70) (2015).
[10] T.K. Kim, S. Noh, S.H. Kang, et al., Current status and future prospective of advanced radiation resistant oxide dispersion strengthened steel (ARROS) development for nuclear reactor system applications [J], Nucl. Eng. Technol. 48 (2) (2016) 572–594.
[11] C. Wei, Z. Zhang, D. Cheng, et al., An overview of laser-based multiple metallic material additive manufacturing: from macro- to micro-scales [J], Intern. J. Extreme Manufact. 3 (1) (2020).
[12] S. Kundu, D. Roy, S. Chatterjee, et al., Influence of interface microstructure on the mechanical properties of titanium/17-4 PH stainless steel solid state diffusion bonded joints [J], Mater. Des. 37 (560–8) (2012).
[13] J. Zhang, D. Long, L. Yu, et al., Microstructure and tensile strength of the bonded interfaces and parent materials in W/ODS steel joints fabricated by direct SSDB [J], Metall. Mater. Trans. A 52 (8) (2021) 3647–3660.
[14] N. Oono, S. Noh, N. Iwata, et al., Microstructures of brazed and solid-state diffusion bonded joints of tungsten with oxide dispersion strengthened steel [J], J. Nucl. Mater. 417 (1–3) (2011) 253–256.
[15] K. Ishida, Y. Gao, K. Nagatsuka, et al., Microstructures and mechanical properties of friction stir welded lap joints of commercially pure titanium and 304 stainless steel [J], J. Alloys Compd. 630 (172–7) (2015).
[16] Q. Chu, M. Zhang, J. Li, et al., Experimental and numerical investigation of microstructure and mechanical behavior of titanium/steel interfaces prepared by explosive welding [J], Mater. Sci. Eng. A 689 (323–31) (2017).
[17] T. Weber, J. Aktaa, Numerical assessment of functionally graded tungsten/steel joints for divertor applications [J], Fusion Eng. Design 86 (2–3) (2011) 220–226.
[18] D. Navaei, X.R. Wang, M. Tillack, et al., Elastic–plastic analysis of the steel-to-tungsten transition joint for a high performance divertor [J], Fusion Eng. Design 88 (5) (2013) 361–367.
[19] J. Yin, D. Wang, L. Yang, et al., Correlation between forming quality and spatter dynamics in laser powder bed fusion [J], Addit. Manuf. 31((2020).
[20] C. Wei, L. Li, X. Zhang, et al., 3D printing of multiple metallic materials via modified selective laser melting [J], CIRP Ann. 67 (1) (2018) 245–248.
[21] C. Wei, Z. Sun, Q. Chen, et al., Additive manufacturing of horizontal and 3D functionally graded 316L/Cu10Sn components via multiple material selective laser melting [J], J. Manuf. Sci. Eng. 141 (8) (2019).
[22] K. Chen, C. Wang, Q. Hong, et al., Selective laser melting 316L/CuSn10 multi-materials: processing optimization, interfacial characterization and mechanical property [J], J. Mater. Process. Technol. (2020) 283(.
[23] B. Li, C. Han, C.W.J. Lim, et al., Interface formation and deformation behaviors of an additively manufactured nickel-aluminum-bronze/15-5 PH multimaterial via laser-powder directed energy deposition [J], Mater. Sci. Eng. A (2022) 829(.
[24] H. Gu, C. Wei, L. Li, et al., Multi-physics modelling of molten pool development and track formation in multi-track, multi-layer and multi-material selective laser melting [J], Int. J. Heat Mass Transf. (2020) 151(.
[25] W.W. Wits, E. Amsterdam, Graded structures by multi-material mixing in laser powder bed fusion [J], CIRP Ann. 70 (1) (2021) 159–162.
[26] B. Guimarães, A. Guedes, C.M. Fernandes, et al., WC-Co/316L stainless steel joining by laser powder bed fusion for multi-material cutting tools manufacturing [J], Int. J. Refract. Met. Hard Mater. 112 (2023).
[27] L. Basílio, B. Guimarães, Ó. Carvalho, et al., WC–co/316L stainless steel bonding enhancement by laser surface texturing and pressure-assisted sintering [J], Int. J. Adv. Manuf. Technol. 128 (9–10) (2023) 4189–4206.
[28] C. Tan, K. Zhou, W. Ma, et al., Selective laser melting of high-performance pure tungsten: parameter design, densification behavior and mechanical properties [J], Sci. Technol. Adv. Mater. 19 (1) (2018) 370–380.
[29] J. Braun, L. Kaserer, J. Stajkovic, et al., Molybdenum and tungsten manufactured by selective laser melting: analysis of defect structure and solidification mechanisms [J], Int. J. Refract. Met. Hard Mater. (2019) 84(.
[30] Y. Zhong, L. Liu, J. Zou, et al., Oxide dispersion strengthened stainless steel 316L with superior strength and ductility by selective laser melting [J], J. Mater. Sci. Technol. 42 (97–105) (2020).
[31] S. Bonk, M. Dürrschnabel, H. Neuberger, et al., Microstructural features in additively manufactured EUROFER97 components [J], Fusion Eng. Des. 173((2021).
[32] Z. Hu, Y. Zhao, K. Guan, et al., Pure tungsten and oxide dispersion strengthened tungsten manufactured by selective laser melting: Microstructure and cracking mechanism [J], Add. Manufact. 36((2020).
[33] A. Bandyopadhyay, Y. Zhang, B. Onuike, Additive manufacturing of bimetallic structures [J], Virtual Phys. Prototyp. 17 (2) (2022) 256–294.
[34] Y. Zhou, L. Duan, F. Li, et al., Effect of heat treatment on the microstructure and mechanical property of W/316L multi-material fabricated by selective laser melting [J], J. Alloys Compd. 890 (2022).
[35] C. Wei, H. Gu, Y. Gu, et al., Abnormal interfacial bonding mechanisms of multi-material additive-manufactured tungsten–stainless steel sandwich structure [J], Intern. J. Extreme Manufact. 4 (2) (2022).
[36] W. Jiang, Z. Xia, J. Xu, et al., Optimization mechanism of bonding strength of laser melting deposited tungsten/reduced activation steel heterogeneous interface via addition of Y2O3 by magnetron sputtering [J], Fusion Engineering and Design (2020) 157.
[37] M. Guo, D. Gu, L. Xi, et al., Selective laser melting additive manufacturing of pure tungsten: role of volumetric energy density on densification, microstructure and mechanical properties [J], Int. J. Refract. Met. Hard Mater. (2019) 84.
[38] M. Miyagi, J. Wang, Keyhole dynamics and morphology visualized by in-situ X-ray imaging in laser melting of austenitic stainless steel [J], J. Mater. Process. Technol. (2020) 282(.
[39] S. Wen, C. Wang, Y. Zhou, et al., High-density tungsten fabricated by selective laser melting: densification, microstructure, mechanical and thermal performance [J], Optics Laser Technol. 116 (128–38) (2019).
[40] L. Wang, Y. Zhang, H.Y. Chia, et al., Mechanism of keyhole pore formation in metal additive manufacturing [J], npj Comput. Mater. 8 (1) (2022).
[41] W.E. King, H.D. Barth, V.M. Castillo, et al., Observation of keyhole-mode laser melting in laser powder-bed fusion additive manufacturing [J], J. Mater. Process. Technol. 214 (12) (2014) 2915–2925.
[42] V. Thampy, A.Y. Fong, N.P. Calta, et al., Subsurface cooling rates and microstructural response during laser based metal additive manufacturing [J], Sci. Rep. 10 (1) (2020).
[43] U. Scipioni Bertoli, G. Guss, S. Wu, et al., In-situ characterization of laser-powder interaction and cooling rates through high-speed imaging of powder bed fusion additive manufacturing [J], Mater. Des. 135 (385–96) (2017).
[44] J. Xie, H. Lu, J. Lu, et al., Additive manufacturing of tungsten using directed energy deposition for potential nuclear fusion application [J], Surf. Coat. Technol. 409 (2021).
[45] X.-Y. Liu, Y. Sui, J.-B. Li, et al., Laser metal deposited steel alloys with uniform microstructures and improved properties prepared by addition of small amounts of dispersed Y2O3 nanoparticles [J], Mater. Sci. Eng. A 806((2021).
[46] Zhanbo Suna, Xiaoping Songa, Z H, G L, et al., Effects of rare earth additions on GMR of melt-spun Cu–Co–Ni ribbons [J], J. Magn. Magn. Mater. (2001) 279–283.
[47] H.Y. Ruiliang Bao, Chuanzhong Chen, Qing Dong, The effect of rare earths on the structure and performance of laser clad coatings [J], Surf. Rev. Lett. 13 (4) (2006) 509–517.
[48] Q. Li, J. Ning, L. Chen, et al., The mechanical response and microstructural evolution of 2195 Al–li alloy during hot tensile deformation [J], J. Alloys Compd. (2020) 848.
[49] C. Wei, L. Liu, Y. Gu, et al., Multi-material additive-manufacturing of tungsten - copper alloy bimetallic structure with a stainless-steel interlayer and associated bonding mechanisms [J], Addit. Manuf. (2022) 50(.

[50] C. Tan, K. Zhou, T. Kuang, Selective laser melting of tungsten-copper functionally graded material [J], Mater. Lett. 237 (328–31) (2019).
[51] A.K. Singh, Y. Mundada, P. Bajaj, et al., Investigation of temperature distribution and solidification morphology in multilayered directed energy deposition of Al-0.5Sc-0.5Si alloy [J], Int. J. Heat Mass Transf. (2022) 186(.
[52] P. Bidare, I. Bitharas, R.M. Ward, et al., Fluid and particle dynamics in laser powder bed fusion [J], Acta Mater. 142 (107–20) (2018).
[53] P.A. Hooper, Melt pool temperature and cooling rates in laser powder bed fusion [J], Addit. Manuf. 22 (548–59) (2018).
[54] I.B. Ozsoy, G. Li, H. Choi, et al., Shape effects on nanoparticle engulfment for metal matrix nanocomposites [J], J. Cryst. Growth 422 (62–8) (2015).
[55] H.J. Chang, H.Y. Cho, J.H. Kim, Stability of Y–Ti–O nanoparticles during laser melting of advanced oxide dispersion-strengthened steel powder, J. Alloys Compd. 653 (528–33) (2015).
[56] L. Barnard, G.R. Odette, I. Szlufarska, et al., An ab initio study of Ti–Y–O nanocluster energetics in nanostructured ferritic alloys [J], Acta Mater. 60 (3) (2012) 935–947.
[57] Z. Hu, K. Guan, Z. Qian, et al., Simultaneous enhancement of strength and ductility in selective laser melting manufactured 316L alloy by employing Y2O3 coated spherical powder as precursor [J], J. Alloys Compd. (2022) 899(.
[58] D. Zhang, D. Qiu, S. Zhu, et al., Grain refinement in laser remelted Mg-3Nd-1Gd-0.5Zr alloy [J], Scr. Mater. 183 (12–6) (2020).
[59] M.J. Bermingham, D.H. Stjohn, J. Krynen, et al., Promoting the columnar to equiaxed transition and grain refinement of titanium alloys during additive manufacturing [J], Acta Mater. 168 (261–74) (2019).
[60] B. Vrancken, R.K. Ganeriwala, M.J. Matthews, Analysis of laser-induced microcracking in tungsten under additive manufacturing conditions: experiment and simulation [J], Acta Mater. 194 (464–72) (2020).
[61] Y. Huang, T.G. Fleming, S.J. Clark, et al., Keyhole fluctuation and pore formation mechanisms during laser powder bed fusion additive manufacturing [J], Nat. Commun. 13 (1) (2022).
[62] N. Kouraytem, X. Li, R. Cunningham, et al., Effect of laser-matter interaction on molten pool flow and keyhole dynamics [J], Phys. Rev. Appl. 11 (6) (2019).